Are Vanadium Intermediates Suitable Mimics in Non-Heme Iron Enzymes? An Electronic Structure Analysis

Vyshnavi Vennelakanti[1,2], Rimsha Mehmood[1,2], and Heather J. Kulik[1,*]

[1]*Department of Chemical Engineering, Massachusetts Institute of Technology, Cambridge, MA 02139, USA*

[2]*Department of Chemistry, Massachusetts Institute of Technology, Cambridge, MA 02139, USA*

ABSTRACT: Vanadyl intermediates are frequently used as mimics for the fleeting Fe(IV)=O intermediate in non-heme iron enzymes that catalyze C–H activation. Using density functional theory and correlated wavefunction theory, we investigate the degree to which the electronic structure of vanadium mimics is comparable to that of catalytic iron intermediates. Our calculations reveal crucial structural and energetic differences between vanadyl and ferryl intermediates primarily due to the former having a low-spin ground state and the latter having a high-spin one. This difference in spin state leads to differences in energetics for accessing isomers that confer activity in non-heme hydroxylase and halogenase enzymes. While interconversion between monodentate and bidentate succinate isomers of the key metal-oxo/hydroxo intermediates is energetically favorable for Fe, it is strongly unfavorable in V mimics. Additionally, isomerization of a terminal metal-oxo between an axial and equatorial position is energetically unfavorable for Fe but favorable for V. Analyses of binding strengths of Fe and V intermediates to α-ketoglutarate and succinate co-substrates reveal that both co-substrates bind more strongly to V than Fe. Given their increasingly frequent use by the biochemistry community of V-based intermediates as mimics, our work highlights the limitations of this approach in studies of non-heme iron enzymes.

Keywords: Non-heme iron, vanadium mimics, density functional theory, metal-oxos, C–H activation

1. Introduction.

Selective C–H activation is essential[1] for the synthesis of bioactive molecules[2-4] and natural products[5-13], medicinal chemistry[3, 14-17], the materials industry[18-20], and agriculture[21-23]. Synthetic routes to activate unreactive C–H bonds require harsh conditions[24] and usually show poor selectivity[25] owing to the high dissociation energy of the C–H bond and its inertness due to low polarity[26]. Biological systems, such as non-heme iron enzymes,[27-34] carry out selective C–H activation of unreactive C–H bonds[35-41] efficiently at ambient conditions to catalyze a wide variety of reactions[37, 42-44]. These enzymes[37, 42-46] play a crucial role in numerous biosynthetic processes[47-52] such as primary and secondary metabolism in plants[42], generation of clinically relevant natural products[44, 53], DNA repair[54-57] and transcription[58-60].

The active site of the α-ketoglutarate (αKG)-dependent non-heme iron halogenases[27-34] is similar to that of hydroxylases[29, 61] where chloride replaces the carboxylate of the canonical 2-His-1-carboxylate facial triad[28, 62, 63] bound to an Fe center. The Fe(IV)–oxo and Fe(III)–hydroxo intermediates formed during the catalytic cycle of these enzymes are highly reactive[44, 64-68] which makes them hard to isolate and characterize with crystallography[69, 70] or spectroscopy[69, 71-74]. An experimental approach to structurally characterize these fleeting Fe(IV)–oxo and Fe(III)–hydroxo intermediates[67, 75] is to replace them with vanadium intermediates that are more inert but are still likely to form octahedral coordination complexes (Figure 1). A search of the protein data bank (PDB)[76] confirms the existence of numerous crystal structures of the resting state intermediate of Fe(II)/αKG enzymes[28, 32] but the absence of an Fe(IV)–oxo intermediate with succinate and two coordinating His residues (Figure 1). However, numerous crystal structures of non-native V(IV)–oxo intermediates have been obtained for non-heme oxygenases[67, 75, 77, 78] and hydroxylases[79] (Figure 1). While these vanadyl intermediates are easier to characterize

experimentally, comparing the metal–ligand (M–L) bond distances between to those for iron reveals considerable differences. For example, the equatorial Fe–N_{His} distance is significantly longer (i.e., beyond the positional uncertainty in the crystal structure[80]) than the V–N_{His} distance (by 0.15 Å) despite comparable axial M–N_{His} distances (M=Fe, V, Figure 1).

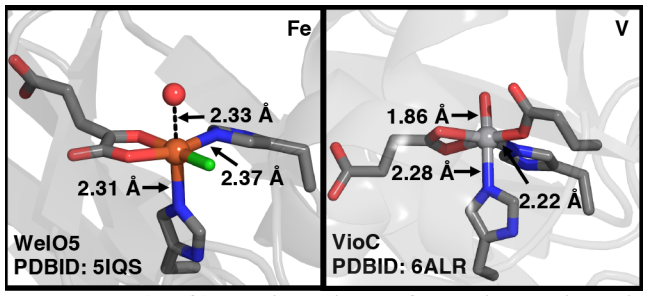

Figure 1. (Left) Active sites of non-heme iron halogenase, WelO5 (PDB ID: 5IQS) and (right) vanadyl mimic of the non-heme iron hydroxylase, VioC (PDB ID: 6ALR). The metal–ligand distances between Fe and water, Fe and His (both axial and equatorial), V and oxo, and V and His (both axial and equatorial) are indicated. Carbon, nitrogen, oxygen, chlorine, vanadium, and iron are shown in gray, blue, red, green, silver, and brown, respectively.

Prior computational[81, 82] and experimental[83, 84] studies have suggested that one or both of the fleeting Fe(IV)–oxo and Fe(III)–hydroxo intermediates formed before and after hydrogen atom abstraction, respectively, could isomerize to explain how halogenases favor halogenation over hydroxylation. Isomerization of the active site in non-heme iron halogenases has also sometimes been proposed to rationalize unexpected substrate positioning, substrate-specific reaction rates, and selectivity[32, 84]. While the crystal structures obtained with Fe(II)/αKG suggest the formation of axial oxo[28, 32, 85] in most enzymes, isomerization to equatorial oxo has been proposed to be possible[40, 83]. Because it is hard to capture these fleeting intermediates experimentally, numerous computational studies[81, 82, 86-91] have been carried out to investigate the mechanism of selective halogenation by non-heme iron halogenases. Even within halogenases, computational or experimental studies have both favored and disfavored isomerization as a necessary step in halogenation in a manner that depends on the enzyme and its substrate. For

instance, while axial oxo appears favored in the carrier-dependent halogenase SyrB2 without any need for isomerization[28, 40, 81], equatorial oxo has been suggested in others such as the carrier-free WelO5, and the need for isomerization has been less clear in the carrier-free BesD halogenase.[32, 85, 91] Although enzymes that natively use iron have been structurally characterized with vanadium metal centers[67, 75, 77-79], no computational studies have assessed the relative energetics for isomerization in the native enzymes and V-based mimics.

Iron-containing catalysts are known to exhibit spin-state-dependent reactivity.[72, 92-101] Non-heme iron halogenases and hydroxylases are believed to react in the high-spin (HS) ground state[65, 66, 91, 102]. In comparison to the electronic structure of mid-row Fe(IV)[66, 81-83, 87, 103], the earlier V(IV)[104] differs in electron configuration, resulting in different accessible spin states. While d^4 ferryl intermediates can access low-spin (LS) singlet, intermediate-spin (IS) triplet, and HS quintet states[65-66] and are expected to prefer HS quintet states, d^1 vanadyl intermediates can only access an LS doublet state[67, 75]. Additionally, it is unknown whether the spin is conserved in V(IV)–oxo and V(III)–hydroxo intermediates formed along the catalytic cycle.

Given the increasing adoption by the biochemistry community of vanadyl mimics for the fleeting ferryl intermediates in C–H activation[67, 75, 77-79], we demonstrate in this work that this experimental approach has severe limitations. We use density functional theory (DFT) and highly accurate correlated wavefunction theory (WFT) to evaluate both the most stable isomers of Fe and V intermediates as well as their isomerization energy landscapes. We show that the most stable isomers for the metal-oxo intermediate and the energetic differences between monodentate and bidentate succinate isomers differ significantly between ferryl and vanadyl intermediates. While the Fe(IV)–oxo isomerization reaction coordinate exhibits a high energy barrier, the corresponding isomerization is barrierless for the vanadyl intermediate. These

differences, which can be attributed to the difference in spin and electron configuration of the metal, also lead to differences in binding strength of co-substrates such as succinate and αKG. Taken together, our studies suggest caution in literal interpretation of vanadyl structures as faithful mimics of ferryl intermediates in mechanistic enzymology.

2. Reaction Mechanism.

Several studies have led to the proposal of a mechanism and likely intermediates[28, 29, 42, 44, 105] in the catalytic cycle for non-heme iron halogenases. Starting from the resting state (**1**), the active site consists of an Fe(II) coordinated to two His ligands, a chloride ligand, a bidentate αKG ligand, and a water molecule which is loosely bound to the metal, producing a 6-coordinate active site (Figure 2). Upon the entry of substrate into the binding pocket, the water molecule is displaced (**2**), and molecular oxygen (**3**) binds to the active site (Figure 2). Once bound, molecular oxygen attacks the carbonyl carbon of αKG, leading to oxidative decarboxylation of αKG and O–O bond cleavage (Figure 2). This step results in the release of a carbon dioxide molecule and an active site consisting of a terminal Fe(IV)–oxo intermediate coordinated to a succinate (**4**) co-substrate (Figure 2). The highly reactive Fe(IV)–oxo intermediate abstracts a hydrogen atom from the substrate, forming a radical substrate and an Fe(III)–OH intermediate (**5**) (Figure 2). This step is followed by rebound halogenation of the substrate radical by the chloride ligand to return of the active site to its resting state (**1**).

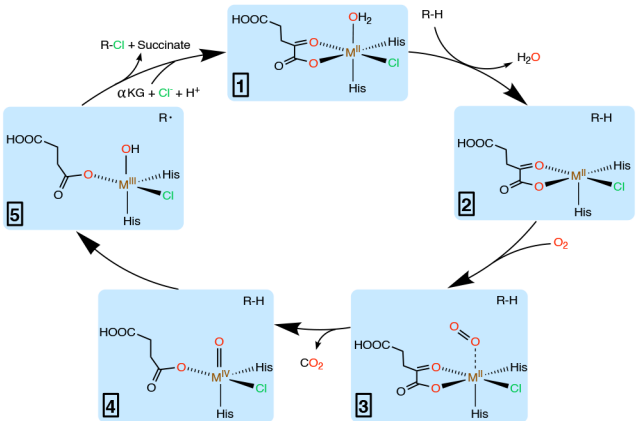

Figure 2. Proposed reaction mechanism of non-heme halogenases (clockwise, starting from the top): the active site with water loosely bound to metal (**1**), water displaced from the active site when the substrate, R–H, enters the active site pocket (**2**), O_2 weakly coordinating the active site (**3**), oxo and succinate (**4**), and hydroxo bound to metal (**5**) are shown. The metal, M = V or Fe, is shown in brown and the metal oxidation state for each intermediate is specified.

While this mechanism is largely agreed upon, the orientation of intermediates in the active site throughout the catalytic cycle as well as the degree of coordination by the αKG or succinate co-substrate has been debated[82, 83, 87, 106]. For instance, in intermediates (**1**) or (**3**), the respective H_2O or O_2 moieties can be present in the axial or equatorial positions, giving rise to axial or equatorial configurational isomers (Supporting Information Figure S1). For the intermediates in the catalytic cycle after oxidative decarboxylation, succinate can bind the metal in either a monodentate or bidentate fashion. As a result, intermediates (**4**) and (**5**) have six possible isomers because the succinate can coordinate the metal in either a monodentate or bidentate configuration, while oxo or hydroxo moieties can occupy equatorial or axial positions, as can the chloride ligand (Supporting Information Figure S1).

3. Results and Discussion.

3.1. Differences in Spin State Distinguish Fe Intermediates from their V-based Mimics.

While fleeting Fe intermediates[67, 75] have been modeled with more inert V-based mimics, differences in electron configurations of Fe and V (e.g., d^4 Fe(IV) vs d^1 V(IV)) mean that intermediates will favor different spin states and have distinct electronic properties (Supporting Information Table S1). This difference may be expected to affect which isomers are the most favorable between V and Fe intermediates. To understand the effect of spin state on geometries, energies, and isomer stabilities of intermediates, we study active site isomers for both Fe and V in their corresponding LS, IS, and HS (for Fe only) states (Supporting Information Table S1, Text S1, and Figure S2). As could be expected from past experimental and computational studies[44, 66, 107], all Fe intermediates (i.e., whether Fe(II)–H_2O or Fe(IV)=O) prefer an HS ground state. On the contrary, the preference for LS versus IS states alternates in V intermediates, i.e., with IS for V(II)–H_2O and V(III)–OH, and LS for V(II)$^{\cdots}O_2$ (alternatively referred to as V(III)–O_2) and V(IV)=O intermediates (Supporting Information Table S2).

The preference for LS and IS states in V intermediates can be expected to lead to shorter M–L bond lengths with the reacting moiety than for HS Fe. Indeed, the favored (i.e., LS or IS) V intermediates have M–L bond lengths with the reacting moiety that are always shorter (by 0.11 Å on average) than the HS Fe intermediates (Supporting Information Table S3). This is not a consequence of differences in size because V has a comparable covalent radius to HS Fe (i.e., 1.53 vs 1.52 Å). In contrast, V–Cl bonds are slightly longer than Fe–Cl bonds (by 0.03–0.08 Å), suggesting that the V–Cl bond is slightly weaker in all four intermediates (Supporting Information Tables S3–S4). While both M–N_{His} (N of His) bonds (M = Fe, V) are comparable for most isomers, the V–N_{His} or V–O_{suc} (O of succinate) bond opposite V–oxo is much longer than the other V–N_{His} or V–O_{suc} bond by ca. 0.30 Å in V(IV)=O isomers (Supporting Information Tables S3–S4 and Figure S3). Because we carried out these optimizations in the gas

phase on cluster models amenable to WFT modeling, we also considered whether inclusion of screening effects from the protein environment could influence these conclusions. We find that inclusion of environment effects (i.e., with implicit solvent models) alters most gas-phase geometries very little (< 0.10 Å) except for the monodentate succinate, equatorial Fe(IV)=O, axial Cl^- isomer where the implicitly solvated Cl–Fe–N_{His} angle is larger by 16° (Supporting Information Table S5 and Figure S4).

Because vanadium is most frequently used to mimic the reactive Fe(IV)=O intermediate immediately prior to hydrogen atom transfer (HAT), relative isomer energetics for both the M(IV)=O and M(III)–OH intermediates must be comparable in order for vanadium to be viewed as a faithful mimic. Because these intermediates form after oxidative decarboxylation of αKG, the carboxylate of the succinate co-substrate can bind the metal in a bidentate or monodentate fashion. While we attempt to compare six potential isomers for both M(IV)=O and M(III)–OH intermediates (i.e., with different positions of the reacting moiety as well as monodentate vs bidentate succinate), some of the monodentate structures rapidly optimize into a bidentate structure or otherwise cannot be stabilized. Thus, we focus on the relative energetics of four M(IV)=O isomers and five M(III)–OH isomers (Supporting Information Text S2 and Figure S5). For Fe, the relative energy of monodentate isomers is only slightly (i.e., 3–8 kcal/mol) higher than the bidentate cases, indicating the possibility that bidentate-to-monodentate interconversion could be accessible (Figure 3 and Supporting Information Figure S1). In contrast, the monodentate isomers of V intermediates are in most cases much less favorable: e.g., for the axial M(IV)=O isomer by 18 kcal/mol (Figure 3).

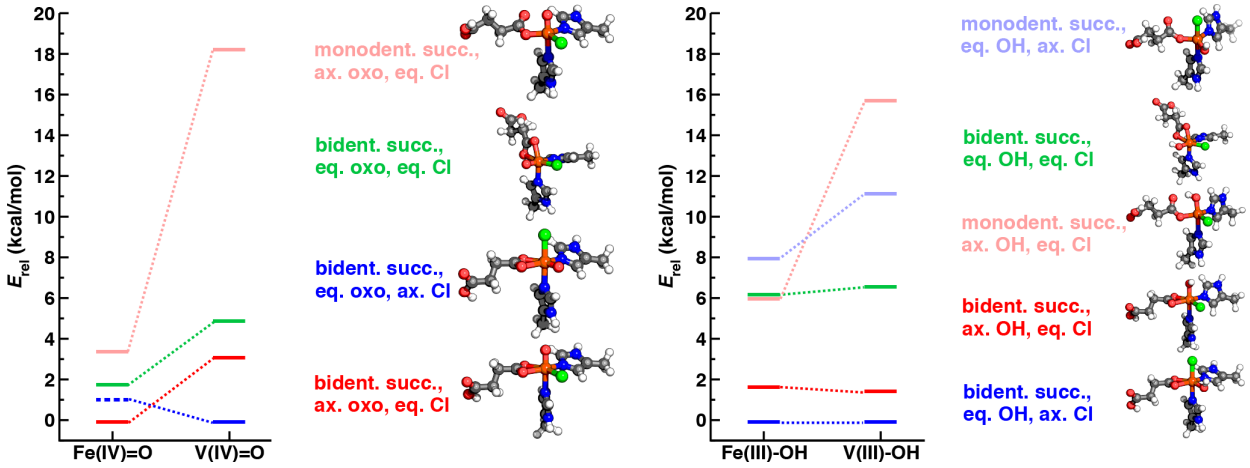

Figure 3. DLPNO/CBS energies (E_{rel}) of isomers of (left) M(IV)=O and (right) M(III)–OH (M = Fe, V) intermediates shown relative to the most stable isomer for each intermediate. Representative structures of Fe(IV)=O and Fe(III)–OH isomers are shown in the insets and labeled. (Top to bottom, left) Isomers are axial (ax.) oxo, equatorial (eq.) Cl, monodentate (monodent.) succinate (succ.); equatorial oxo and Cl, bidentate (bident.) succinate; axial Cl, equatorial oxo, bidentate succinate; axial oxo, equatorial Cl, bidentate succinate. (Top to bottom, right) Isomers are axial Cl, equatorial OH, monodentate succinate; equatorial OH and Cl, bidentate succinate; axial OH, equatorial Cl, monodentate succinate; axial OH, equatorial Cl, bidentate succinate; axial Cl, equatorial OH, bidentate succinate. The dashed blue line corresponds to an estimated DLPNO/CBS energy. Hydrogen, carbon, nitrogen, oxygen, chlorine, and iron are shown in white, gray, blue, red, green, and brown, respectively.

In addition to differences in preference for succinate binding, there are differences in preferred configurational isomers for Fe versus V (Figure 3). While all bidentate isomers are fairly comparable in energy for Fe with the axial M(IV)=O isomer slightly favored, an equatorial M(IV)=O isomer with axial Cl^- is preferred for V (Figure 3). Although differences are significant for the M(IV)=O moieties, isomer energetics after the HAT step are more similar for the M(III)–OH intermediates where the relative energetics of the three lowest-energy bidentate isomers of Fe and V intermediates are comparable (Figure 3 and Supporting Information Figure S1).

To determine whether the differences between Fe(IV)=O and V(IV)=O intermediates are a result of the effect of the metal identity or the spin state, we next compare the corresponding isomers between intermediates with similar spin states. Metal-oxo bond lengths of IS Fe(IV)=O

and LS V(IV)=O are comparable (i.e., within < 0.05 Å), and all other M–L distances differ by < 0.20 Å except for specific isomers that have elongated V–N_{His} or V–O_{suc} bonds (Supporting Information Table S6). The isomer energetics for IS triplet Fe(IV)=O are also comparable to those of LS doublet V(IV)=O. Both IS Fe(IV)=O and LS V(IV)=O have a strong preference for the bidentate succinate isomer, which is stabilized by ca. 16 and 18 kcal/mol, respectively, over the monodentate succinate with an axial oxo (Supporting Information Figure S6). Among the bidentate succinate isomers, both Fe and V species show a moderate preference for equatorial oxo and axial Cl^- over axial oxo (ca. 3 kcal/mol, Supporting Information Figure S6). Thus, the differences between HS Fe(IV)=O and LS V(IV)=O are largely a consequence of differences in their respective spin states (Supporting Information Text S3).

To understand how configurational isomer preference for each metal affects other parts of the catalytic cycle, we also studied the two axial and equatorial isomers of M(II)–H_2O and M(III)–O_2 (M=Fe, V) intermediates with bidentate αKG (Supporting Information Figure S1). All M(II)–H_2O intermediates are characterized by comparably long (≥ 2.20 Å) M(II)–H_2O bond lengths indicative of a weak interaction consistent with observations from literature[32, 108, 109], but the equatorial isomer is weakly favored (i.e., by 2.1 kcal/mol for Fe and 3.6 kcal/mol for V) (Supporting Information Figures S1 and S7, and Table S3). Both (i.e., Fe and V) M(III)–O_2 axial and equatorial isomers optimize to precursor structures in which O_2 attacks the carboxylate carbon of αKG, and they have comparable energetics (Supporting Information Figures S1 and S7 and Table S7).

Thus, analysis of the ground spin state, geometries and preferred isomers indicates that there are significant differences between Fe and V active site isomers that are most apparent for the M(IV)=O intermediate where V is most essential as a mimic of Fe. This will strongly impact

the interpretation of studies using V(IV)=O intermediates as mimics for fleeting Fe(IV)=O intermediates.

3.2. Metal-oxo Isomerization Energy Landscapes.

We next compared the isomerization energy landscapes of the M(IV)=O intermediate for both Fe and V in detail because isomerization of the fleeting Fe(IV)=O intermediate has been invoked as a factor in determining the selectivity of functionalization subsequent to C–H activation[67, 75]. Our analysis of active site isomers (see Sec. 3.1) showed that the energetic difference between monodentate and bidentate succinate isomers for Fe(IV)=O is small (ca 3 kcal/mol). While the bidentate succinate isomer is slightly more stable than the monodentate succinate isomer, we study active site isomerization using monodentate isomers as it ensures the needed coordination flexibility in the active site to enable isomerization of the reacting moiety. We compare the native case of Fe and its V mimic because we aim to understand if the V mimic is both a suitable structural mimic of the metal-oxo, which has been proposed experimentally[67], as well as whether the metal-oxo in the native system may rearrange in a manner that differs from the V mimic.

We study two isomerization reaction coordinates (RCs) for monodentate succinate isomers of M(IV)–oxo intermediates. The first RC corresponds to isomerization between equatorial oxo and axial oxo in which Cl^- remains equatorial. This isomerization is captured by the change in N_{His}–M=O angle with the His trans to the axial oxo (Figures 4a and 4c). For the iron species along this RC, we observe two minima: the global minimum for axial oxo and a local minimum for the equatorial oxo separated by a large barrier (ca. 8 kcal/mol) for isomerization (Figure 4a). We characterize the transition state (N_{His}–Fe=O angle: 127°) along

this pathway by confirming a single imaginary frequency of ca. 132 cm^{-1} along the RC. In contrast, a single minimum is observed along the RC with V (Figure 4a). While for Fe, the global minimum (N_{His}–Fe=O angle: 172°) closely resembles the axial oxo isomer, the global minimum for V (N_{His}–V=O angle: 148°) shifts away from this geometry (Figure 4a). As a result, this V-containing structure positions the oxo midway between the equatorial plane and the axial position (Figure 4c). We observe that the RC energy landscape is qualitatively unchanged if all degrees of freedom are constrained in the V mimic to their values in the Fe model (Supporting Information Figure S8). In some enzymes, it has been proposed[32, 85] that equatorial positioning of the oxo moiety is a factor that determines the selectivity of the enzymatic reaction. However, our results cast doubt on the utility of vanadyl structural mimics to assess this proposal. Our observations demonstrate that the relative stability of the axial oxo and the high energy barrier for isomerization in non-heme Fe halogenases are not captured by V mimics.

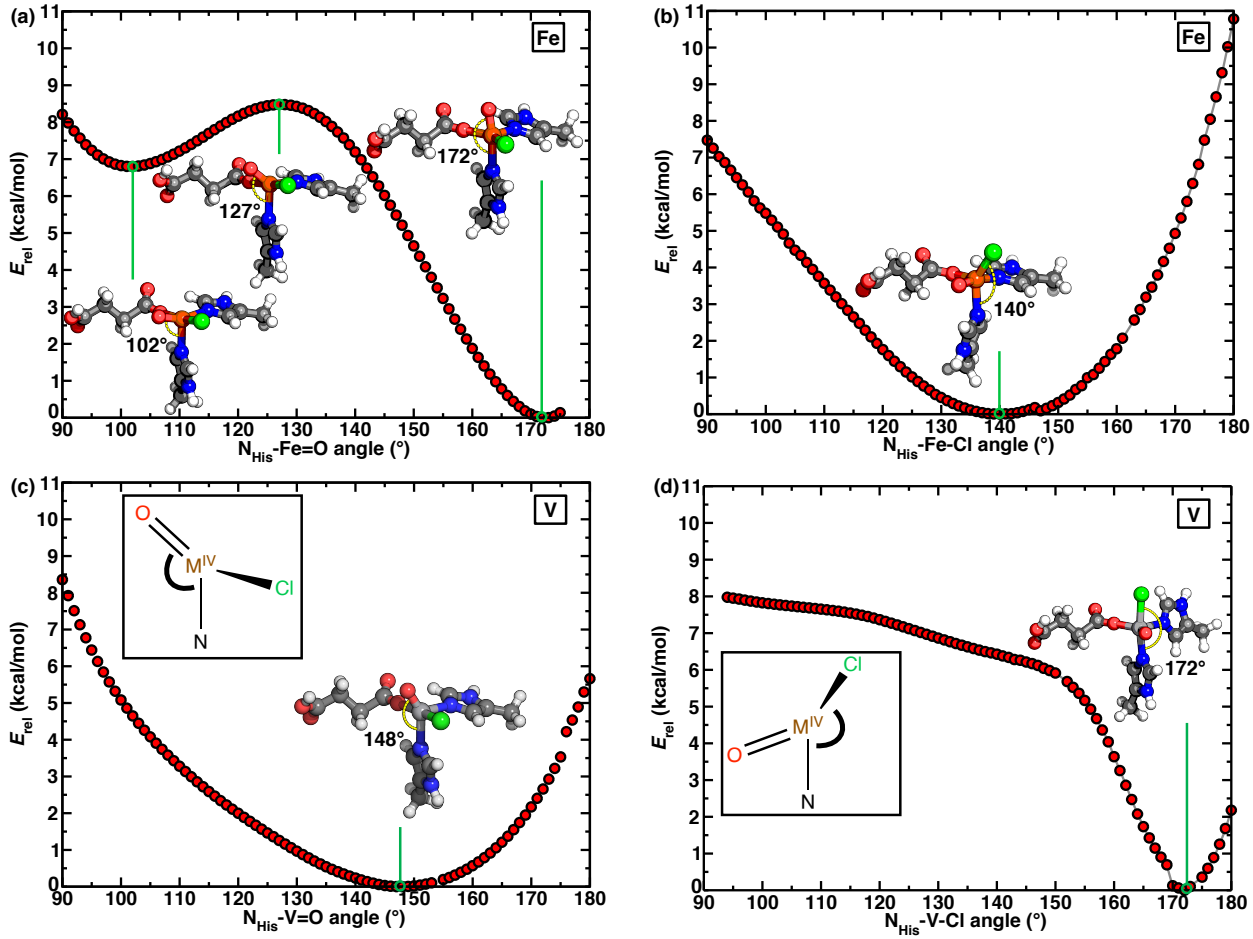

Figure 4. Reaction coordinates for isomerization between equatorial oxo and axial oxo (left: (a), (c)), and equatorial chloride and axial chloride (right: (b), (d)) with monodentate succinate for Fe (top: (a), (b)) and V (bottom: (c), (d)) active sites. The geometries corresponding to minima and transition states are shown as insets. The N_{His}–M–Cl and N_{His}–M=O angles (in °, M=Fe, V) are indicated as yellow dashed curves in the insets along with skeleton structures that show the corresponding angles in the bottom plots. Hydrogen, carbon, nitrogen, oxygen, chlorine, vanadium, and iron are shown in white, gray, blue, red, green, silver, and brown, respectively.

The second isomerization RC we explore connects the isomers of equatorial Cl^- and axial Cl^- with equatorial oxo (Figures 4b and 4d). We again model this RC with monodentate succinate for flexibility, and we describe the RC as a function of N_{His}–M–Cl angle, with the His that is trans to the axial moiety (Figures 4b and 4d). Here, the Fe(IV)=O intermediate has a single minimum energy structure with the Cl^- tilted (N_{His}–M–Cl angle: 140°) out of the equatorial plane (Figure 4b). The V(IV)=O RC obtained by single-point calculations of the

structures from the Fe(IV)=O RC shares a similar minimum energy structure with Fe (Supporting Information Figure S9). However, we observe a small approximate barrier (ca. 2 kcal/mol) between the global minimum and the equatorial Cl^- structure that was absent for Fe (Supporting Information Figure S9). We characterize the transition state (N_{His}–V–Cl angle: 116°) on the V(IV)=O RC by observing a primary imaginary frequency of 69 cm^{-1} along the angular RC mode. If we instead allow all but the RC coordinate to relax for V(IV)=O, we observe significant differences from both the Fe(IV)=O RC and its isostructural V(IV)=O RC (Figure 4d). Here, we observe a steep energy landscape with a global minimum energy structure (N_{His}–V–Cl angle: 172°) that is similar to the axial Cl^- isomer (Figure 4d).

Further examination of the relaxed Fe and V RCs reveals that the significant differences can be attributed to the position of the oxo moiety in the equatorial plane (Supporting Information Figures S10–S11). We observe that the angle formed by succinate, Fe, and oxo (O_{suc}–Fe=O) in the equatorial plane changes more significantly along the RC for V (86–145°) than for Fe (86–110°), resulting in an O_{suc}–V=O angle that is ca. 40° larger than the O_{suc}–Fe=O angle observed in the minimum energy structures along the relaxed RCs (Supporting Information Figure S10). This difference could be attributed to the fact that the fully relaxed V structure becomes more trigonal bipyramidal in nature, whereas the Fe model remains square pyramidal (Figure 4). This indicates that potential isomerization from equatorial to axial Cl^- , which has been invoked to explain selectivity for halogenation, would either be barrierless leading to axial Cl^- as global minimum or have a small energy barrier for the V(IV)=O mimics depending on the rigidity of the protein environment (Figure 4). In contrast, for Fe, this transition is always barrierless and the minimum energy structure positions Cl^- midway between the equatorial plane and axial position (Figure 4). Thus, for systems where oxo is expected to be in the equatorial

position during halogenation[32, 85], the behavior of non-heme Fe halogenases is not accurately captured by vanadium mimics, which lead to either predictions of a different minimum energy structure or the presence of a small energy barrier.

We also study an isomerization RC connecting equatorial hydroxo and axial hydroxo structures in which Cl^- remains equatorial. This isomerization is captured by the change in N_{His}–M–OH angle with the His trans to the axial hydroxo (Supporting Information Figure S12). While both Fe and V RCs are qualitatively similar with one global minimum, the minimum energy structures exhibit different N_{His}–M–OH angles, with the Fe intermediate having a ca. 10° larger angle than the V intermediate (Supporting Information Figure S12). Comparison of this RC with the one connecting equatorial and axial oxo reveals significant differences for Fe but qualitatively similar landscapes for V (Figure 4 and Supporting Information Figure S12). This indicates that while an axial Fe(IV)=O is preferred, the Fe(III)–OH intermediate formed after hydrogen atom transfer favors a hydroxo intermediate that tilts away (N_{His}–Fe–OH = 154°) from the axial orientation, and this difference in orientation preference is larger for Fe than the V mimic.

Overall, we observe that angular RCs and energy landscapes differ significantly between Fe and V systems, likely due to the differences in spin states between HS quintet Fe(IV)=O and LS doublet V(IV)=O intermediates, suggesting that observations from crystal structures of vanadyl mimics may not be reflective of the favored Fe intermediates during catalysis. Our observations also suggest that hydrogen atom transfer to form the metal-hydroxo species alters isomer stability in a fashion for Fe that is also not captured by V mimics of this intermediate. Taken together, these observations highlight the limits of using LS/IS vanadium-based

intermediates as mimics in experimental studies of fleeting HS iron intermediates in non-heme iron enzymes.

3.3 Binding Strength of Co-Substrates in Fe and V Active Sites.

Formation of a monodentate succinate is critical to isomerization for M(IV)=O and M(III)–OH intermediates (see Sec. 3.2), but bidentate succinate configurations are generally more stable than monodentate succinate for both Fe and V intermediates (Figure 3). To quantify these differences in both binding configurations and with metal centers, we evaluated a quantum mechanical measurement of bond order (i.e., the Mayer bond order[110]) to determine relative binding strengths of different orientations of succinate in comparison to αKG, which consistently binds in a bidentate configuration.

Although αKG is always bound in a bidentate fashion, its binding strength can vary by intermediate. The binding strength of αKG to Fe in HS O_2-bound isomers is twice that observed for HS water-bound isomers (Mayer bond order: 1.23 vs 0.49), suggesting a key role of the axial moiety in determining the binding strength of αKG (Figure 5). We observe a similar trend for ground spin state V intermediates, where αKG binds more strongly to V in LS O_2-bound isomers than in IS H_2O-bound isomers (Mayer bond order: 1.69 vs 0.92, Figure 5 and Supporting Information Figure S13). Overall, αKG binds more strongly to V than Fe in corresponding intermediates, likely due to the preferred LS/IS ground state for V in comparison to the HS ground state for Fe intermediates (Figure 5).

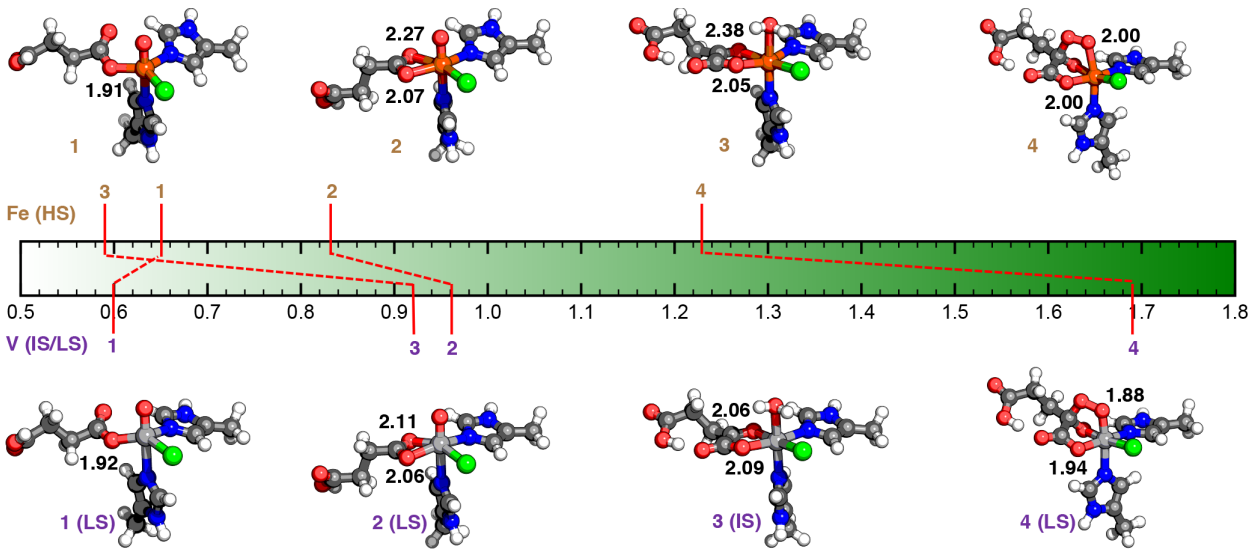

Figure 5. Scale demonstrating the Mayer bond orders of metal–succinate bonds of ground state high-spin (HS) Fe (top) and intermediate-spin/low-spin (IS/LS) V (bottom) intermediates with monodentate and bidentate succinate. The four intermediates shown in the figure are (1) M(IV)=O with monodentate succinate, (2) M(IV)=O with bidentate succinate, (3) M(II)–H_2O with bidentate αKG, and (4) M(III)–O_2 with bidentate αKG. The corresponding M–O (of succinate/αKG) bond lengths (in Å) are indicated in the insets. Hydrogen, carbon, nitrogen, oxygen, chlorine, vanadium, and iron are shown in white, gray, blue, red, green, silver, and brown, respectively.

Because bidentate-to-monodentate variations are expected to be most critical in isomerization of the M(IV)=O intermediate, we quantified the relative bond order in these intermediates for M = V and Fe. The bond order of both monodentate (0.65) and bidentate succinate (0.83) are significantly lower than that of αKG (1.23) for the HS Fe case (Figure 5). The difference between bidentate and monodentate bond order (0.96 vs 0.60) is larger for LS V(IV)=O but bidentate binding strength is still markedly reduced in comparison to αKG (1.69, Figure 5). This difference could explain why formation of the monodentate succinate V(IV)=O intermediate is less favorable than for the Fe(IV)=O case. These differences in bond order could also be anticipated in part based on differences in structure. The M–O distances of Fe/V to both O atoms of αKG are shorter by ca. 0.17 Å in comparison to average M–O distances for bidentate

succinate (Supporting Information Table S8). One of the Fe–O distances for bidentate succinate is much longer than the other (0.20 Å), suggesting an asymmetry in the bond strength, while the difference between V–O distances of bidentate succinate is smaller (0.05 Å, Supporting Information Table S8). While our analysis focuses on the M(IV)=O intermediate evaluated with gas-phase optimized geometries, similar trends hold for the M(III)–OH intermediate formed after HAT as well as upon inclusion of implicit solvent environment during optimization of intermediates (Supporting Information Figures S14–S19). The computed binding energies of αKG and succinate to metal-H_2O/O_2 and metal-oxo intermediates, respectively, also support the observations from bond order analyses (Supporting Information Table S9). We thus conclude that bidentate succinate is only slightly more strongly bound than monodentate succinate in the case of Fe intermediates. This supports the potential isomerization between isomers of M(IV)=O and M(III)–OH intermediates to enable HAT and/or halogenation during the catalytic cycle (see Sec. 3.2).

We next sought to further isolate the effect of bidentate coordination on restricting isomerization of the reacting moiety. We created an artificial isomerization RC with the succinate constrained to its bidentate orientation and compare it to the RC we computed earlier with monodentate succinate (Figures 4 and 6). While the difference between monodentate and bidentate succinate isomers in free optimizations is ca. 3 kcal/mol for Fe and 18 kcal/mol for V, the endpoints (i.e., minima) of the RCs with monodentate or bidentate succinate enforced further destabilize the monodentate RC, especially for Fe (ca. 20 kcal/mol for Fe and 26 kcal/mol for V, Figures 3 and 6). Closer examination reveals that our enforcing the monodentate succinate constraint causes the C–O^-–M angle formed by succinate with the metal to be much larger than the angle observed in free optimizations (by ca. 47° for Fe and 38° for V) (Supporting

Information Figure S20). We indeed observe that the average bond order of geometries along the RC obtained with monodentate succinate is smaller than that of free optimizations (Fe: 0.45 vs 0.65, V: 0.42 vs 0.60) likely due to the unfavorable C–O^-–M angle as a consequence of the constraints employed to separately probe a fully monodentate structure (Supporting Information Figure S21). Thus, in those cases where free optimization is carried out for all degrees of freedom besides the RC, partial bidentate-like character could be forming (Figure 4).

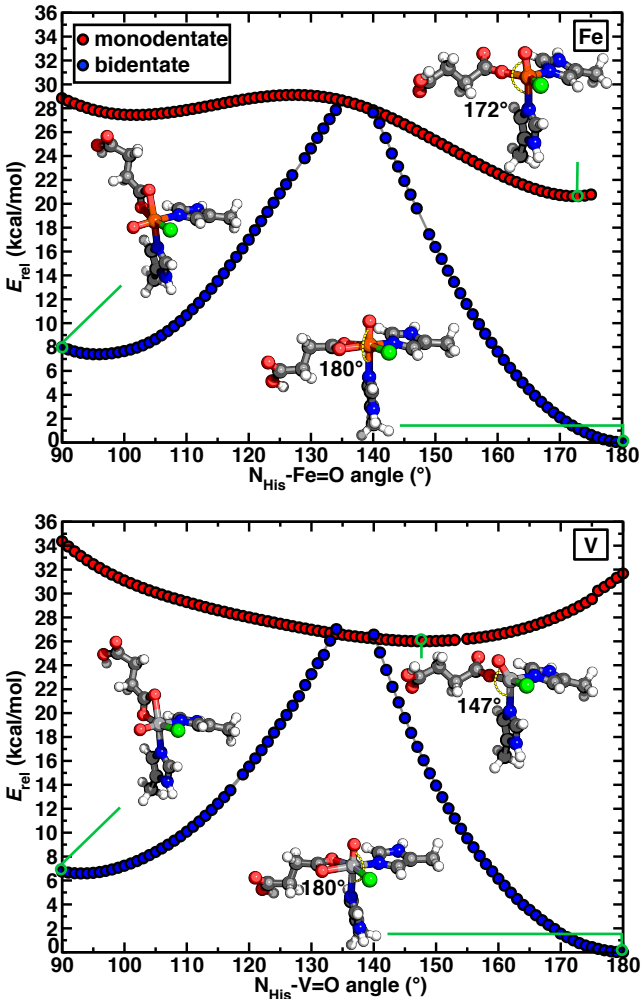

Figure 6. Reaction coordinates for isomerization between equatorial oxo and axial oxo with monodentate succinate (shown in red) and bidentate succinate (shown in blue) for Fe (top) and V (bottom) active sites. The geometries corresponding to minima are shown as insets. The N_{His}–M=O angle (in °, M=Fe, V) is indicated as yellow dashed curves in the insets. Hydrogen, carbon, nitrogen, oxygen, chlorine, vanadium, and iron are shown in white, gray, blue, red, green, silver, and brown, respectively.

While the bidentate succinate is more stable than its monodentate counterpart in local minima, qualitatively bidentate structures are not likely to be feasible throughout the isomerization pathway with either Fe or V (Figure 6). For the portions of the pathway in which the N_{His}–M=O angle is around 130–140°, a bidentate structure cannot be obtained, although one can be reformed for more obtuse angles (Figure 6 and Supporting Information Figure S22). This observation holds whether we attempt to coordinate the succinate only in the equatorial plane or if it were to bind in both the equatorial and axial sites (Supporting Information Figure S22). Thus, isomerization is likely facilitated by the partial weakening of a qualitatively bidentate succinate only temporarily in the RC that causes a lower energetic penalty than fully breaking the second, weaker metal–succinate bond. We indeed observe that the bond orders of geometries along the RC obtained with bidentate succinate decrease slightly in moving from the global minima (ca. 0.85) to an N_{His}–M=O angle of 140° (ca. 0.80), indicating that one of the M–O_{suc} bonds becomes weaker (Supporting Information Figure S21). However, we see an increase in bond order in moving from an N_{His}–M=O angle of 100° (ca. 0.78) to 130° (ca. 0.88) as a result of constraining O_{suc} atoms to ensure bidentate succinate coordination for these geometries (Supporting Information Figure S21). In the absence of these constraints, the M–O_{suc} bond order would likely decrease due to weakening of one of the M–O_{suc} bonds.

4. Conclusions.

While vanadyl is frequently used as a mimic for the fleeting Fe(IV)=O intermediate in C–H activation, we showed through a combination of DFT geometry optimizations and accurate WFT energetics that there are crucial differences between the structure and energetics of ferryl and vanadyl intermediates. These observations can be rationalized by differences in the ground

spin states of Fe- and V-containing species. Crucially, the most favorable bidentate M(IV)=O isomer is different for Fe and V, and the conversion between monodentate and bidentate isomers of the key metal-oxo/hydroxo intermediates is energetically favorable for Fe but strongly unfavorable in vanadyl mimics.

Active site isomerization of monodentate Fe(IV)=O between equatorial and axial oxo isomers, which has been invoked by some mechanistic proposals, was characterized by two minima separated by a transition state (ca. 8 kcal/mol). The corresponding RC for V(IV)=O is significantly different and lacks this barrier, with only one minimum in which oxo is located midway between the equatorial plane and axial position. Additionally, we observed that the Fe RC between equatorial and axial Cl^- isomers has a minimum energy structure that positions Cl^- midway between equatorial plane and axial position. However, isomerization of the corresponding V structure can be either barrierless with axial Cl^- as global minimum or have a small energy barrier (ca. 2 kcal/mol) depending on the rigidity of the protein environment. In contrast to the observation that M(IV)=O RCs are significantly different for Fe and V, Fe(III)–OH and V(III)–OH have qualitatively similar energy landscapes but differing minimum energy structures. These significant differences between Fe and V RCs highlight the limits of using LS/IS V-based intermediates as mimics in studies of fleeting HS Fe intermediates in non-heme iron enzymes. A vanadyl preference for the axial or equatorial isomer does not mean that the ferryl will have that same preference, and barriers for interconversion between the two isomers can be expected to differ between ferryl and vanadyl intermediates.

Because isomerization of the reacting species requires monodentate succinate coordination, we analyzed the relative bond strengths of monodentate and bidentate succinate for Fe and V. We quantified the succinate binding strength to the metal to understand the differences

in monodentate and bidentate succinate binding relative to bidentate αKG. We observed that αKG binds more strongly to V than Fe, likely due to the preferred LS/IS ground state for V. Furthermore, for both Fe and V, bidentate succinate binds with greater strength than monodentate succinate, but weaker than αKG. The RC with bidentate succinate revealed that bidentate structures are not accessible throughout the RC, indicating a weaker metal–succinate bond must form during isomerization. This is indeed supported by the decreased binding strength of bidentate succinate along the RC away from the global minimum.

Overall, our study highlights the limits of using V-based intermediates as mimics in non-heme iron halogenases owing to differences in spin states that result in different geometries, isomer energetics, and isomerization RCs. This study has focused on isomer stability because it is already known that vanadyls are structural mimics that do not carry out hydrogen atom transfer. Nevertheless, a natural follow-up to this work will be to analyze any differences in hydrogen atom transfer reaction coordinates from each of the possible favored isomers of iron.

5. Computational Details.

The active site of a representative non-heme iron halogenase, WelO5[32, 108, 109] (PDB ID: 5IQS), was extracted from the enzyme's crystal structure. The model comprised the Fe metal center, chloride, αKG, water, and two metal-bound His ligands truncated at the sidechain (i.e., excluding Cα and backbone atoms, Supporting Information Figure S23). Hydrogen atoms were added to the extracted active site using Avogadro v1.2.0[111], and the metal-distal carboxylate oxygen of αKG and Nδ atoms of His ligands were also protonated (Supporting Information Figure S23). The final active site model had an overall neutral charge. All added hydrogen atoms were optimized with the UFF force field[112] while the heavy atoms were held fixed. The isomers

of the active site containing water, O_2, oxo, or hydroxo, and succinate (monodentate or bidentate with succinate tail protonated) ligands were generated with molSimplify[113], which uses OpenBabel[114, 115] as a backend. The iron metal center was replaced by vanadium to generate similar initial geometries with a vanadium metal center.

All constrained geometry optimizations were performed with density functional theory (DFT) using the generalized gradient approximation (GGA) global hybrid PBE0[116] (with 25% exchange) and the def2-TZVP basis set[117] using ORCA[118] v.4.0.1.2 and v.4.2.1. For these optimizations, PBE0 was augmented with the semi-empirical D3[119] dispersion correction using Becke-Johnson[120] damping. All optimizations were carried out in redundant internal coordinates using the BFGS algorithm with default thresholds of 3×10^{-4} hartree/bohr for the maximum gradient and 5×10^{-6} hartree for the change in self-consistent field (SCF) energy between steps. For all optimizations, the methyl carbon atoms of His ligands and five of the heavy atoms of succinate (i.e., excluding the carboxylate that coordinates the metal) were held fixed to mimic the succinate and His positions of the VioC structure (Supporting Information Figure S24). The five heavy atoms of succinate were held fixed after observing the freely optimized structure to rearrange (i.e., curl on itself) in a manner that would not be feasible in the protein environment, whereas αKG was optimized freely because it did not undergo similar rearrangements (Supporting Information Figure S25). Singlet calculations were carried out in a spin-restricted formalism while all other spin states were simulated with unrestricted calculations (Supporting Information Tables S1–S2).

Geometry optimizations of the active site isomers were carried out in both gas-phase and implicit solvent with two solvent dielectric values, $\varepsilon = 10$ and 80, approximately mimicking the protein[121] and an aqueous environment, respectively. The implicit solvent optimizations were

carried out using the conductor-like polarizable continuum model[122] (C-PCM) solvation energies in combination with the conductor-like screening solvent model (COSMO) epsilon function type obtained at the PBE0/def2-TZVP level of theory. All initial and optimized structures for both gas phase and implicit solvent optimizations are provided in the Supporting Information.

Initial geometries to generate RCs were constructed from the PBE0/def2-TZVP optimized geometries of active site isomers using an in-house Python script. The isomerization RCs were sampled by rotating oxo and/or chloride ligands with respect to the axial His ligand in 1° increments of the angle formed by oxo/chloride, metal center (i.e., Fe, V), and nitrogen of the axial His (Supporting Information Text S4 and Figure S26). This was followed by constrained optimizations along the chosen RC for both iron and vanadium metal centers (Supporting Information Text S4). Single-point calculations were also carried out at the PBE0/def2-TZVP level of theory on optimized geometries with the iron metal center by replacing iron with vanadium to understand the effect of different metal centers for a given geometry. High-energy structures along the PBE0/def2-TZVP optimized RCs were used to obtain vibrational frequencies. Numerical Hessian calculations were carried out at the PBE0/def2-TZVP level of theory where the Hessian was computed using the central difference approach after 6*N* atomic displacements with ORCA v.4.0.1.2. The presence of an imaginary frequency along the RC confirmed that the high-energy structure corresponded to a transition state.

Single-point energy calculations on the PBE0/def2-TZVP geometries of various active site isomers were carried out at the domain-localized pair natural orbital coupled cluster level of theory with single, double and perturbative triples (i.e., DLPNO-CCSD(T)[123, 124]) using ORCA v4.0.1.2. Dunning-style correlation consistent double-ζ and triple-ζ (i.e., aug-cc-pVDZ and aug-cc-pVTZ) basis sets were employed to enable two-point[125-127] extrapolation to the complete basis

set (CBS) limit. All reported DLPNO-CCSD(T) energies were obtained using tight PNO thresholds (Supporting Information Table S10). Multiwfn[128] was used to perform Mayer bond order analysis to quantify the strength of binding of αKG, monodentate, and bidentate succinate to both iron and vanadium metal centers.

AUTHOR INFORMATION

Corresponding Author

*email:hjkulik@mit.edu

Notes

The authors declare no competing financial interest.

Supporting Information. Isomers of intermediates of the non-heme iron halogenase active site; potential spin states of Fe and V active site intermediates; geometries of different spin states for Fe and V active site intermediates; optimized geometries of Fe(IV)=O in different spin states; DLPNO-CCSD(T)/CBS spin splitting energies for isomers of all intermediates; optimized metal-ligand bond lengths of representative isomers of Fe and V; Mayer's bond orders of representative active site isomers of Fe and V; isomers of V(IV)=O showing elongated V–N_{His} or V–O_{suc} bonds; differences between implicit solvent and gas-phase metal–ligand bond lengths; gas-phase and implicit solvent optimized geometries of the Fe(IV)=O isomer; convergence of isomers to appropriate geometries; initial and optimized geometries of M(IV)=O and M(III)–OH isomers; differences between IS Fe and LS V metal–ligand bond lengths of M(IV)=O; DLPNO-CCSD(T)/CBS energies of IS Fe(IV)=O and LS V(IV)=O isomers; comparison of IS/LS Fe intermediates to IS/LS V intermediates; optimized geometries of M(II)–H_2O and M(III)–O_2 isomers; DLPNO-CCSD(T)/CBS relative energies of M(II)–H_2O, M(III)–O_2 isomers; isomerization RC between equatorial and axial oxo for V(IV)=O; isomerization RC between equatorial and axial Cl^- for V(IV)=O; O_{suc}–M=O angle as a function of isomerization RC angle N_{His}–M–Cl^-; V(IV)=O isomerization RC between eq. and ax. Cl^- with extra constraints; isomerization RC between equatorial and axial hydroxo for M(III)–OH; bond order scale of HS Fe and LS V intermediates in gas-phase; metal–ligand bond lengths for intermediates shown in Figure 5; bond order scale of ground spin state Fe and V intermediates in gas-phase; bond order scale of HS Fe and LS V intermediates in gas-phase; bond order scale of the ground state Fe and V intermediates in implicit solvent; bond order scale of HS Fe and LS V intermediates in implicit solvent; stable M(IV)=O geometries from free and constrained optimizations; M–O bond orders of geometries along Fe and V isomerization RCs; representative structure along isomerization RC; extracted active site of WelO5; representative structure showing constrained atoms in

optimizations; details of reaction coordinate construction; representative structures showing reaction coordinate angles; tight PNO default thresholds used for DLPNO-CCSD(T) calculations (PDF)

Initial geometries, gas-phase optimized geometries, and implicit solvent optimized geometries of isomers of Fe and V active site intermediates; initial and optimized geometries along Fe and V isomerization reaction coordinates for equatorial and axial oxo isomerization as well as equatorial and axial chloride isomerization (ZIP)

ACKNOWLEDGMENT

This work was supported by the National Science Foundation under grant numbers CBET-1704266 and CBET-1846426. The authors acknowledge the MIT SuperCloud and Lincoln Laboratory Supercomputing Center for providing HPC resources that have contributed to the research results reported within this paper. This work also made use of Department of Defense HPCMP computing resources. This work was also carried out in part using computational resources from the Extreme Science and Engineering Discovery Environment (XSEDE), which is supported by National Science Foundation grant number ACI-1548562. H.J.K. holds a Career Award at the Scientific Interface from the Burroughs Wellcome Fund, an AAAS Marion Milligan Mason Award, and an Alfred P. Sloan Fellowship in Chemistry, which supported this work. The authors acknowledge Akash Bajaj, Aditya Nandy, Azadeh Nazemi, and Adam H. Steeves for providing critical readings of the manuscript.

REFERENCES

1. Gandeepan, P.; Muller, T.; Zell, D.; Cera, G.; Warratz, S.; Ackermann, L., 3d Transition Metals for C-H Activation. *Chem. Rev.* **2019,** *119* (4), 2192-2452.
2. Blunt, J. W.; Copp, B. R.; Hu, W.-P.; Munro, M. H.; Northcote, P. T.; Prinsep, M. R., Marine natural products. *Nat. Prod. Rep.* **2009,** *26* (2), 170-244.
3. Nakama, Y.; Yoshida, O.; Yoda, M.; Araki, K.; Sawada, Y.; Nakamura, J.; Xu, S.; Miura, K.; Maki, H.; Arimoto, H., Discovery of a novel series of semisynthetic vancomycin derivatives effective against vancomycin-resistant bacteria. *J. Med. Chem.* **2010,** *53*, 2528-2533.
4. Latham, J.; Brandenburger, E.; Shepherd, S. A.; Menon, B. R.; Micklefield, J., Development of halogenase enzymes for use in synthesis. *Chem. Rev.* **2018,** *118* (1), 232-269.

5. Karimov, R. R.; Hartwig, J. F., Transition-Metal-Catalyzed Selective Functionalization of C(sp(3))-H Bonds in Natural Products. *Angew. Chem., Int. Ed.* **2018,** *57* (16), 4234-4241.
6. Brady, P. B.; Bhat, V., Recent Applications of Rh- and Pd-Catalyzed C(sp(3))-H Functionalization in Natural Product Total Synthesis. *Eur. J. Org. Chem.* **2017,** *2017* (35), 5179-5190.
7. Sinha, S. K.; Zanoni, G.; Maiti, D., Natural Product Synthesis by C-H Activation. *Asian J. Org. Chem.* **2018,** *7* (7), 1178-1192.
8. Qiu, Y. Y.; Gao, S. H., Trends in applying C-H oxidation to the total synthesis of natural products. *Nat. Prod. Rep.* **2016,** *33* (4), 562-581.
9. Yamaguchi, J.; Yamaguchi, A. D.; Itami, K., C-H Bond Functionalization: Emerging Synthetic Tools for Natural Products and Pharmaceuticals. *Angew. Chem., Int. Ed.* **2012,** *51* (36), 8960-9009.
10. Rossi, R.; Lessi, M.; Manzini, C.; Marianetti, G.; Bellina, F., Direct (Hetero) arylation Reactions of (Hetero) arenes as Tools for the Step-and Atom-Economical Synthesis of Biologically Active Unnatural Compounds Including Pharmaceutical Targets. *Synthesis* **2016,** *48* (22), 3821-3862.
11. Chen, D. Y. K.; Youn, S. W., C-H Activation: A Complementary Tool in the Total Synthesis of Complex Natural Products. *Chem. Eur. J.* **2012,** *18* (31), 9452-9474.
12. Cochrane, R. V. K.; Vederas, J. C., Highly Selective but Multifunctional Oxygenases in Secondary Metabolism. *Acc. Chem. Res.* **2014,** *47* (10), 3148-3161.
13. Lewis, J. C.; Coelho, P. S.; Arnold, F. H., Enzymatic functionalization of carbon-hydrogen bonds. *Chem. Soc. Rev.* **2011,** *40* (4), 2003-2021.
14. Seki, M., A New Catalytic System for Ru-Catalyzed C-H Arylation Reactions and Its Application in the Practical Syntheses of Pharmaceutical Agents. *Org. Process Res. Dev.* **2016,** *20* (5), 867-877.
15. Ackermann, L., Robust Ruthenium(II)-Catalyzed C-H Arylations: Carboxylate Assistance for the Efficient Synthesis of Angiotensin-II-Receptor Blockers. *Org. Process Res. Dev.* **2015,** *19* (1), 260-269.
16. Baldwin, J. E.; Bradley, M., Isopenicillin-N Synthase - Mechanistic Studies. *Chem. Rev.* **1990,** *90* (7), 1079-1088.
17. Choroba, O. W.; Williams, D. H.; Spencer, J. B., Biosynthesis of the vancomycin group of antibiotics: Involvement of an unusual dioxygenase in the pathway to (S)-4-hydroxyphenylglycine. *J. Am. Chem. Soc.* **2000,** *122* (22), 5389-5390.
18. Tang, M. L.; Bao, Z. A., Halogenated Materials as Organic Semiconductors. *Chem. Mater.* **2011,** *23* (3), 446-455.
19. Berger, G.; Soubhye, J.; Meyer, F., Halogen bonding in polymer science: from crystal engineering to functional supramolecular polymers and materials. *Polym. Chem.* **2015,** *6* (19), 3559-3580.
20. Amanchukwu, C. V.; Harding, J. R.; Shao-Horn, Y.; Hammond, P. T., Understanding the Chemical Stability of Polymers for Lithium-Air Batteries. *Chem. Mater.* **2015,** *27* (2), 550-561.
21. Jeschke, P., The unique role of fluorine in the design of active ingredients for modern crop protection. *ChemBioChem* **2004,** *5* (5), 570-589.
22. Jeschke, P., The unique role of halogen substituents in the design of modern agrochemicals. *Pest Manage. Sci.* **2010,** *66* (1), 10-27.

23. Hubrich, J.; Himmler, T.; Rodefeld, L.; Ackermannt, L., Ruthenium(II)-Catalyzed C-H Arylation of Azoarenes by Carboxylate Assistance. *ACS Catal.* **2015,** *5* (7), 4089-4093.
24. Prakash, G. S.; Mathew, T.; Hoole, D.; Esteves, P. M.; Wang, Q.; Rasul, G.; Olah, G. A., N-Halosuccinimide/BF3− H2O, efficient electrophilic halogenating systems for aromatics. *J. Am. Chem. Soc.* **2004,** *126* (48), 15770-15776.
25. Alonso, F.; Beletskaya, I. P.; Yus, M., Metal-mediated reductive hydrodehalogenation of organic halides. *Chem. Rev.* **2002,** *102* (11), 4009-4092.
26. Altus, K. M.; Love, J. A., The continuum of carbon-hydrogen (C-H) activation mechanisms and terminology. *Commun. Chem.* **2021,** *4* (1), 173.
27. Vaillancourt, F. H.; Yin, J.; Walsh, C. T., SyrB2 in Syringomycin E Biosynthesis is a Nonheme FeII α-Ketoglutarate- and O2-Dependent Halogenase. *Proc. Natl. Acad. Sci.* **2005,** *102* (29), 10111-10116.
28. Blasiak, L. C.; Vaillancourt, F. H.; Walsh, C. T.; Drennan, C. L., Crystal structure of the non-haem iron halogenase SyrB2 in syringomycin biosynthesis. *Nature* **2006,** *440* (7082), 368-371.
29. Galonić, D. P.; Barr, E. W.; Walsh, C. T.; Bollinger Jr., J. M.; Krebs, C., Two Interconverting Fe(IV) Intermediates in Aliphatic Chlorination by the Halogenase CytC3. *Nat. Chem. Biol.* **2007,** *3* (2), 113-116.
30. Wong, C.; Fujimori, D. G.; Walsh, C. T.; Drennan, C. L., Structural analysis of an open active site conformation of nonheme iron halogenase CytC3. *J. Am. Chem. Soc.* **2009,** *131* (13), 4872-4879.
31. Vaillancourt, F. H.; Yeh, E.; Vosburg, D. A.; O'connor, S. E.; Walsh, C. T., Cryptic chlorination by a non-haem iron enzyme during cyclopropyl amino acid biosynthesis. *Nature* **2005,** *436* (7054), 1191.
32. Mitchell, A. J.; Zhu, Q.; Maggiolo, A. O.; Ananth, N. R.; Hillwig, M. L.; Liu, X.; Boal, A. K., Structural Basis for Halogenation by Iron- and 2-oxo-glutarate-dependent Enzyme WelO5. *Nat. Chem. Biol.* **2016,** *12* (8), 636-640.
33. Khare, D.; Wang, B.; Gu, L.; Razelun, J.; Sherman, D. H.; Gerwick, W. H.; Håkansson, K.; Smith, J. L., Conformational switch triggered by α-ketoglutarate in a halogenase of curacin A biosynthesis. *Proc. Natl. Acad. Sci.* **2010,** *107* (32), 14099-14104.
34. Pratter, S. M.; Light, K. M.; Solomon, E. I.; Straganz, G. D., The role of chloride in the mechanism of O2 activation at the mononuclear nonheme Fe (II) center of the halogenase HctB. *J. Am. Chem. Soc.* **2014,** *136* (26), 9385-9395.
35. Kovaleva, E. G.; Lipscomb, J. D., Versatility of biological non-heme Fe(II) centers in oxygen activation reactions. *Nat. Chem. Biol.* **2008,** *4* (3), 186-193.
36. Capyk, J. K.; D'Angelo, I.; Strynadka, N. C.; Eltis, L. D., Characterization of 3-Ketosteroid 9 alpha-Hydroxylase, a Rieske Oxygenase in the Cholesterol Degradation Pathway of Mycobacterium tuberculosis. *J. Biol. Chem.* **2009,** *284* (15), 9937-9946.
37. Costas, M.; Mehn, M. P.; Jensen, M. P.; Que Jr, L., Dioxygen activation at mononuclear nonheme iron active sites: enzymes, models, and intermediates. *Chem. Rev.* **2004,** *104* (2), 939-986.
38. Busby, R. W.; Townsend, C. A., A single monomeric iron center in clavaminate synthase catalyzes three nonsuccessive oxidative transformations. *Bioorg. Med. Chem.* **1996,** *4* (7), 1059-1064.
39. Joseph, C. A.; Maroney, M. J., Cysteine dioxygenase: structure and mechanism. *Chem. Commun.* **2007,** (32), 3338-3349.

40. Matthews, M. L.; Krest, C. M.; Barr, E. W.; Vaillancourt, F. H.; Walsh, C. T.; Green, M. T.; Krebs, C.; Bollinger, J. M., Substrate-Triggered Formation and Remarkable Stability of the C-H Bond-Cleaving Chloroferryl Intermediate in the Aliphatic Halogenase, SyrB2. *Biochemistry* **2009,** *48* (20), 4331-4343.
41. Lloyd, M. D.; Lee, H. J.; Harlos, K.; Zhang, Z. H.; Baldwin, J. E.; Schofield, C. J.; Charnock, J. M.; Garner, C. D.; Hara, T.; van Scheltinga, A. C. T.; Valegard, K.; Viklund, J. A. C.; Hajdu, J.; Andersson, I.; Danielsson, A.; Bhikhabhai, R., Studies on the active site of deacetoxycephalosporin C synthase. *J. Mol. Biol.* **1999,** *287* (5), 943-960.
42. Hausinger, R. P., Fe(II)/alpha-ketoglutarate-dependent hydroxylases and related enzymes. *Crit. Rev. Biochem. Mol. Biol.* **2004,** *39* (1), 21-68.
43. Solomon, E. I.; Light, K. M.; Liu, L. V.; Srnec, M.; Wong, S. D., Geometric and electronic structure contributions to function in non-heme iron enzymes. *Acc. Chem. Res.* **2013,** *46* (11), 2725-2739.
44. Krebs, C.; Fujimori, D. G.; Walsh, C. T.; Bollinger, J. M., Non-heme Fe(IV)-oxo intermediates. *Acc. Chem. Res.* **2007,** *40* (7), 484-492.
45. Solomon, E. I.; Goudarzi, S.; Sutherlin, K. D., O2 activation by non-heme iron enzymes. *Biochemistry* **2016,** *55* (46), 6363–6374.
46. Timmins, A.; de Visser, S. P., A Comparative Review on the Catalytic Mechanism of Nonheme Iron Hydroxylases and Halogenases. *Catalysts* **2018,** *8* (8), 314.
47. Kivirikko, K. I.; Myllyharju, J., Prolyl 4-hydroxylases and their protein disulfide isomerase subunit. *Matrix Biology* **1998,** *16* (7), 357-368.
48. Ivan, M.; Kondo, K.; Yang, H.; Kim, W.; Valiando, J.; Ohh, M.; Salic, A.; Asara, J. M.; Lane, W. S.; Kaelin, W. G., Jr., HIFα targeted for VHL-mediated destruction by proline hydroxylation: Implications for O2 sensing. *Science* **2001,** *292* (5516), 464-468.
49. Jaakkola, P.; Mole, D. R.; Tian, Y.-M.; Wilson, M. I.; Gielbert, J.; Gaskell, S. J.; von Kriegsheim, A.; Hebestreit, H. F.; Mukherji, M.; Schofield, C. J.; Maxwell, P. H.; Pugh, C. W.; Ratcliffe, P. J., Targeting of HIF-α to the von Hippel-Lindau ubiquitylation complex by O2-regulated prolyl hydroxylation. *Science* **2001,** *292* (5516), 468-472.
50. Gerken, T.; Girard, C. A.; Tung, Y.-C. L.; Webby, C. J.; Saudek, V.; Hewitson, K. S.; Yeo, G. S. H.; McDonough, M. A.; Cunliffe, S.; McNeill, L. A.; Galvanovskis, J.; Rorsman, P.; Robins, P.; Prieur, X.; Coll, A. P.; Ma, M.; Jovanovic, Z.; Farooqi, I. S.; Sedgwick, B.; Barroso, I.; Lindahl, T.; Ponting, C. P.; Ashcroft, F. M.; O'Rahilly, S.; Schofield, C. J., The Obesity-Associated FTO Gene Encodes a 2-Oxoglutarate-Dependent Nucleic Acid Demethylase. *Science* **2007,** *318* (5855), 1469-1472.
51. Que, L.; Ho, R. Y. N., Dioxygen activation by enzymes with mononuclear non-heme iron active sites. *Chem. Rev.* **1996,** *96* (7), 2607-2624.
52. Ryle, M. J.; Hausinger, R. P., Non-heme iron oxygenases. *Curr. Opin. Chem. Biol.* **2002,** *6* (2), 193-201.
53. Walsh, C. T., The chemical versatility of natural-product assembly lines. *Acc. Chem. Res.* **2008,** *41* (1), 4-10.
54. Trewick, S. C.; Henshaw, T. F.; Hausinger, R. P.; Lindahl, T.; Sedgwick, B., Oxidative demethylation by Escherichia coli AlkB directly reverts DNA base damage. *Nature* **2002,** *419* (6903), 174-178.
55. Falnes, P. O.; Johansen, R. F.; Seeberg, E., AlkB-mediated oxidative demethylation reverses DNA damage in Escherichia coli. *Nature* **2002,** *419* (6903), 178-182.

56. Yi, C.; Jia, G.; Hou, G.; Dai, Q.; Zhang, W.; Zheng, G.; Jian, X.; Yang, C.-G.; Cui, Q.; He, C., Iron-Catalysed Oxidation Intermediates Captured in a DNA Repair Dioxygenase. *Nature* **2010,** *468* (7321), 330-333.
57. Duncan, T.; Trewick, S. C.; Koivisto, P.; Bates, P. A.; Lindahl, T.; Sedgwick, B., Reversal of DNA alkylation damage by two human dioxygenases. *Proc. Natl. Acad. Sci.* **2002,** *99* (26), 16660-16665.
58. Cloos, P. A. C.; Christensen, J.; Agger, K.; Maiolica, A.; Rappsilber, J.; Antal, T.; Hansen, K. H.; Helin, K., The putative oncogene GASC1 demethylates tri- and dimethylated lysine 9 on histone H3. *Nature* **2006,** *442* (7100), 307-311.
59. Klose, R. J.; Yamane, K.; Bae, Y.; Zhang, D.; Erdjument-Bromage, H.; Tempst, P.; Wong, J.; Zhang, Y., The transcriptional repressor JHDM3A demethylates trimethyl histone H3 lysine 9 and lysine 36. *Nature* **2006,** *442* (7100), 312-316.
60. Tsukada, Y.-i.; Fang, J.; Erdjument-Bromage, H.; Warren, M. E.; Borchers, C. H.; Tempst, P.; Zhang, Y., Histone demethylation by a family of JmjC domain-containing proteins. *Nature* **2006,** *439* (7078), 811-816.
61. Mitchell, A. J.; Dunham, N. P.; Bergman, J. A.; Wang, B.; Zhu, Q.; Chang, W.-c.; Liu, X.; Boal, A. K., Structure-guided reprogramming of a hydroxylase to halogenate its small molecule substrate. *Biochemistry* **2017,** *56* (3), 441-444.
62. Koehntop, K. D.; Emerson, J. P.; Que, L., The 2-His-1-carboxylate facial triad: a versatile platform for dioxygen activation by mononuclear non-heme iron (II) enzymes. *JBIC, J. Biol. Inorg. Chem.* **2005,** *10* (2), 87-93.
63. Que Jr, L., One motif—many different reactions. *Nat. Struct. Mol. Biol.* **2000,** *7* (3), 182.
64. Groves, J. T., Key elements of the chemistry of cytochrome P-450: The oxygen rebound mechanism. *J. Chem. Educ.* **1985,** *62*, 928.
65. Price, J. C.; Barr, E. W.; Glass, T. E.; Krebs, C.; Bollinger, J. M., Evidence for hydrogen abstraction from C1 of taurine by the high-spin Fe(IV) intermediate detected during oxygen activation by taurine :alpha-ketoglutarate dioxygenase (TauD). *J. Am. Chem. Soc.* **2003,** *125* (43), 13008-13009.
66. Price, J. C.; Barr, E. W.; Tirupati, B.; Bollinger, J. M.; Krebs, C., The first direct characterization of a high-valent iron intermediate in the reaction of an alpha-ketoglutarate-dependent dioxygenase: A high-spin Fe(IV) complex in taurine/alpha-ketoglutarate dioxygenase (TauD) from Escherichia coli (vol 42, pg 7497, 2003). *Biochemistry* **2004,** *43* (4), 1134-1134.
67. Martinie, R. J.; Pollock, C. J.; Matthews, M. L.; Bollinger, J. M.; Krebs, C.; Silakov, A., Vanadyl as a Stable Structural Mimic of Reactive Ferryl Intermediates in Mononuclear Nonheme-Iron Enzymes. *Inorg. Chem.* **2017,** *56* (21), 13382-13389.
68. Bollinger Jr, J. M.; Krebs, C., Stalking intermediates in oxygen activation by iron enzymes: Motivation and method. *J. Inorg. Biochem.* **2006,** *100* (4), 586-605.
69. Rohde, J. U.; In, J. H.; Lim, M. H.; Brennessel, W. W.; Bukowski, M. R.; Stubna, A.; Munck, E.; Nam, W.; Que, L., Crystallographic and spectroscopic characterization of a nonheme Fe(IV)=O complex. *Science* **2003,** *299* (5609), 1037-1039.
70. Klinker, E. J.; Kaizer, J.; Brennessel, W. W.; Woodrum, N. L.; Cramer, C. J.; Que, L., Structures of nonheme oxoiron(IV) complexes from x-ray crystallography, NMR spectroscopy, and DFT calculations. *Angew. Chem., Int. Ed.* **2005,** *44* (24), 3690-3694.
71. Rohde, J. U.; Torelli, S.; Shan, X. P.; Lim, M. H.; Klinker, E. J.; Kaizer, J.; Chen, K.; Nam, W. W.; Que, L., Structural insights into nonheme alkylperoxoiron(III) and oxoiron(IV) intermediates by x-ray absorption spectroscopy. *J. Am. Chem. Soc.* **2004,** *126* (51), 16750-16761.

72. Pestovsky, O.; Stoian, S.; Bominaar, E. L.; Shan, X. P.; Munck, E.; Que, L.; Bakac, A., Aqueous Fe-IV=O: Spectroscopic identification and oxo-group exchange. *Angew. Chem., Int. Ed.* **2005,** *44* (42), 6871-6874.
73. Grapperhaus, C. A.; Mienert, B.; Bill, E.; Weyhermuller, T.; Wieghardt, K., Mononuclear (nitrido)iron(V) and (oxo)iron(IV) complexes via photolysis of [(cyclam-acetato)Fe-III(N-3)](+) and ozonolysis of [(cyclam-acetato)Fe-III(O3SCF3)](+) in water/acetone mixtures. *Inorg. Chem.* **2000,** *39* (23), 5306-5317.
74. Ehudin, M. A.; Gee, L. B.; Sabuncu, S.; Braun, A.; Moenne-Loccoz, P.; Hedman, B.; Hodgson, K. O.; Solomon, E. I.; Karlin, K. D., Tuning the Geometric and Electronic Structure of Synthetic High-Valent Heme Iron(IV)-Oxo Models in the Presence of a Lewis Acid and Various Axial Ligands. *J. Am. Chem. Soc.* **2019,** *141* (14), 5942-5960.
75. Davis, K. M.; Altmyer, M.; Martinie, R. J.; Schaperdoth, I.; Krebs, C.; Bollinger, J. M.; Boal, A. K., Structure of a Ferryl Mimic in the Archetypal Iron(II)- and 2-(Oxo)-glutarate-Dependent Dioxygenase, TauD. *Biochemistry* **2019,** *58* (41), 4218-4223.
76. Berman, H. M.; Westbrook, J.; Feng, Z.; Gilliland, G.; Bhat, T. N.; Weissig, H.; Shindyalov, I. N.; Bourne, P. E., The Protein Data Bank. *Nucleic Acids Res.* **2000,** *28* (1), 235-242.
77. Dunham, N. P.; Chang, W. C.; Mitchell, A. J.; Martinie, R. J.; Zhang, B.; Bergman, J. A.; Rajakovich, L. J.; Wang, B.; Silakov, A.; Krebs, C.; Boal, A. K.; Bollinger, J. M., Two Distinct Mechanisms for C-C Desaturation by Iron(II)- and 2-(Oxo)glutarate-Dependent Oxygenases: Importance of alpha-Heteroatom Assistance. *J. Am. Chem. Soc.* **2018,** *140* (23), 7116-7126.
78. Chekan, J. R.; Ongpipattanakul, C.; Wright, T. R.; Zhang, B.; Bollinger, J. M.; Rajakovich, L. J.; Krebs, C.; Cicchillo, R. M.; Nair, S. K., Molecular basis for enantioselective herbicide degradation imparted by aryloxyalkanoate dioxygenases in transgenic plants. *Proc. Natl. Acad. Sci.* **2019,** *116* (27), 13299-13304.
79. Mitchell, A. J.; Dipham, N. P.; Martinie, R. J.; Bergman, J. A.; Pollock, C. J.; Hu, K.; Allen, B. D.; Chang, W.-c.; Silakov, A.; Bollinger Jr., J. M.; Krebs, C.; Boal, A. K., Visualizing the Reaction Cycle in an Iron(II)- and 2-(Oxo)-glutarate-Dependent Hydroxylase. *J. Am. Chem. Soc.* **2017,** *139* (39), 13830-13836.
80. Wilson, K. S.; Butterworth, S.; Dauter, Z.; Lamzin, V. S.; Walsh, M.; Wodak, S.; Pontius, J.; Richelle, J.; Vaguine, A.; Sander, C.; Hooft, R. W. W.; Vriend, G.; Thornton, J. M.; Laskowski, R. A.; MacArthur, M. W.; Dodson, E. J.; Murshudov, G.; Oldfield, T. J.; Kaptein, R.; Rullmann, J. A. C.; Network, E.-D. V., Who Checks the Checkers? Four Validation Tools Applied to Eight Atomic Resolution Structures. *J. Mol. Biol.* **1998,** *276* (2), 417-436.
81. Borowski, T.; Noack, H.; Radon, M.; Zych, K.; Siegbahn, P. E., Mechanism of selective halogenation by SyrB2: a computational study. *J. Am. Chem. Soc.* **2010,** *132* (37), 12887-12898.
82. Huang, J.; Li, C.; Wang, B.; Sharon, D. A.; Wu, W.; Shaik, S., Selective chlorination of substrates by the halogenase SyrB2 is controlled by the protein according to a combined quantum mechanics/molecular mechanics and molecular dynamics study. *Acs Catal* **2016,** *6* (4), 2694-2704.
83. Wong, S. D.; Srnec, M.; Matthews, M. L.; Liu, L. V.; Kwak, Y.; Park, K.; Bell, C. B.; Alp, E. E.; Zhao, J. Y.; Yoda, Y.; Kitao, S.; Seto, M.; Krebs, C.; Bollinger, J. M.; Solomon, E. I., Elucidation of the Fe(IV)=O intermediate in the catalytic cycle of the halogenase SyrB2. *Nature* **2013,** *499* (7458), 320-+.

84. Martinie, R. J.; Livada, J.; Chang, W.-c.; Green, M. T.; Krebs, C.; Bollinger Jr., J. M.; Silakov, A., Experimental Correlation of Substrate Position with Reaction Outcome in the Aliphatic Halogenase, SyrB2. *J. Am. Chem. Soc.* **2015,** *137* (21), 6912-6919.
85. Neugebauer, M. E.; Sumida, K. H.; Pelton, J. G.; McMurry, J. L.; Marchand, J. A.; Chang, M. C. Y., A Family of Radical Halogenases for the Engineering of Amino-Acid-Based Products. *Nat. Chem. Biol.* **2019,** *15* (10), 1009-1016.
86. de Visser, S. P.; Latifi, R., Carbon Dioxide: A Waste Product in the Catalytic Cycle of α-Ketoglutarate Dependent Halogenases Prevents the Formation of Hydroxylated By-Products. *J. Phys. Chem. B* **2009,** *113* (1), 12-14.
87. Kulik, H. J.; Blasiak, L. C.; Marzari, N.; Drennan, C. L., First-Principles Study of Non-heme Fe(II) Halogenase SyrB2 Reactivity. *J. Am. Chem. Soc.* **2009,** *131* (40), 14426-14433.
88. Kulik, H. J.; Drennan, C. L., Substrate placement influences reactivity in non-heme Fe (II) halogenases and hydroxylases. *J. Biol. Chem.* **2013,** *288* (16), 11233-11241.
89. Rugg, G.; Senn, H. M., Formation and structure of the ferryl [Fe=O] intermediate in the non-haem iron halogenase SyrB2: classical and QM/MM modelling agree. *Phys. Chem. Chem. Phys.* **2017,** *19* (44), 30107-30119.
90. Mehmood, R.; Qi, H. W.; Steeves, A. H.; Kulik, H. J., The Protein's Role in Substrate Positioning and Reactivity for Biosynthetic Enzyme Complexes: the Case of SyrB2/SyrB1. *ACS Catal.* **2019,** *9*, 4930-4943.
91. Mehmood, R.; Vennelakanti, V.; Kulik, H. J., Spectroscopically Guided Simulations Reveal Distinct Strategies for Positioning Substrates to Achieve Selectivity in Nonheme Fe(II)/α-Ketoglutarate-Dependent Halogenases. *ACS Catal.* **2021,** *11*, 12394–12408.
92. Hirao, H.; Kumar, D.; Que, L., Jr.; Shaik, S., Two-State Reactivity in Alkane Hydroxylation by Non-Heme Iron-Oxo Complexes. *J. Am. Chem. Soc.* **2006,** *128* (26), 8590-8606.
93. Shaik, S.; Danovich, D.; Fiedler, A.; Schroder, D.; Schwarz, H., 2-State Reactivity in Organometallic Gas-Phase Ion Chemistry. *Helv. Chim. Acta* **1995,** *78* (6), 1393-1407.
94. Schroder, D.; Shaik, S.; Schwarz, H., Two-state reactivity as a new concept in organometallic chemistry. *Acc. Chem. Res.* **2000,** *33* (3), 139-145.
95. Abram, S.-L.; Monte-Perez, I.; Pfaff, F. F.; Farquhar, E. R.; Ray, K., Evidence of Two-State Reactivity in Alkane Hydroxylation by Lewis-Acid Bound Copper-Nitrene Complexes. *Chem. Commun.* **2014,** *50* (69), 9852-9854.
96. Rohde, J. U.; Que, L., Axial coordination of carboxylate activates the non-heme Fe-IV = O unit. *Angew. Chem., Int. Ed.* **2005,** *44* (15), 2255-2258.
97. Bukowski, M. R.; Koehntop, K. D.; Stubna, A.; Bominaar, E. L.; Halfen, J. A.; Munck, E.; Nam, W.; Que, L., A thiolate-ligated nonheme oxoiron(IV) complex relevant to cytochrome P450. *Science* **2005,** *310* (5750), 1000-1002.
98. Decker, A.; Rohde, J. U.; Que, L.; Solomon, E. I., Spectroscopic and quantum chemical characterization of the electronic structure and bonding in a non-heme Fe-IV=O complex. *J. Am. Chem. Soc.* **2004,** *126* (17), 5378-5379.
99. Decker, A.; Solomon, E. I., Comparison of Fe-IV = O heme and non-heme species: Electronic structures, bonding, and reactivities. *Angew. Chem., Int. Ed.* **2005,** *44* (15), 2252-2255.
100. Schoneboom, J. C.; Neese, F.; Thiel, W., Toward identification of the Compound I reactive intermediate in cytochrome P450 chemistry: A QM/MM study of its EPR and Mossbauer parameters. *J. Am. Chem. Soc.* **2005,** *127* (16), 5840-5853.

101. Hohenberger, J.; Ray, K.; Meyer, K., The biology and chemistry of high-valent iron-oxo and iron-nitrido complexes. *Nat. Commun.* **2012,** *3*, 720.
102. Fujimori, D. G.; Barr, E. W.; Matthews, M. L.; Koch, G. M.; Yonce, J. R.; Walsh, C. T.; Bollinger, J. M.; Krebs, C.; Riggs-Gelasco, P. J., Spectroscopic evidence for a high-spin Br-Fe(IV)-Oxo intermediate in the alpha-ketoglutarate-dependent halogenase CytC3 from Streptomyces. *J. Am. Chem. Soc.* **2007,** *129* (44), 13408-+.
103. Pandian, S.; Vincent, M. A.; Hillier, I. H.; Burton, N. A., Why does the enzyme SyrB2 chlorinate, but does not hydroxylate, saturated hydrocarbons? A density functional theory (DFT) study. *Dalton Trans.* **2009,** (31), 6201-6207.
104. Ballhausen, C. J.; Gray, H. B., The Electronic Structure of the Vanadyl Ion. *Inorg. Chem.* **1962,** *1* (1), 111–122.
105. Vaillancourt, F. H.; Yeh, E.; Vosburg, D. A.; Garneau-Tsodikova, S.; Walsh, C. T., Nature's inventory of halogenation catalysts: Oxidative strategies predominate. *Chem. Rev.* **2006,** *106* (8), 3364-3378.
106. Srnec, M.; Wong, S. D.; Matthews, M. L.; Krebs, C.; Bollinger, J. M.; Solomon, E. I., Electronic Structure of the Ferryl Intermediate in the alpha-Ketoglutarate Dependent Non-Heme Iron Halogenase SyrB2: Contributions to H Atom Abstraction Reactivity. *J. Am. Chem. Soc.* **2016,** *138* (15), 5110-5122.
107. Sinnecker, S.; Svensen, N.; Barr, E. W.; Ye, S.; Bollinger, J. M.; Neese, F.; Krebs, C., Spectroscopic and computational evaluation of the structure of the high-spin Fe(IV)-oxo intermediates in taurine: alpha-Ketoglutarate dioxygenase from Escherichia coli and its His99Ala ligand variant. *J. Am. Chem. Soc.* **2007,** *129* (19), 6168-6179.
108. Hillwig, M. L.; Liu, X., A New Family of Iron-Dependent Halogenases Acts on Freestanding Substrates. *Nat. Chem. Biol.* **2014,** *10* (11), 921-923.
109. Hillwig, M. L.; Fuhrman, H. A.; Ittiamornkul, K.; Sevco, T. J.; Kwak, D. H.; Liu, X., Identification and Characterization of a Welwitindolinone Alkaloid Biosynthetic Gene Cluster in the Stigonematalean Cyanobacterium Hapalosiphon welwitschii. *ChemBioChem* **2014,** *15* (5), 665-669.
110. Mayer, I., Bond order and valence indices: A personal account. *J. Comput. Chem.* **2007,** *28* (1), 204-221.
111. Hanwell, M. D.; Curtis, D. E.; Lonie, D. C.; Vandermeersch, T.; Zurek, E.; Hutchison, G. R., Avogadro: an advanced semantic chemical editor, visualization, and analysis platform. *J. Cheminf.* **2012,** *4*, 17.
112. Rappe, A. K.; Casewit, C. J.; Colwell, K. S.; Goddard, W. A. I.; Skiff, W. M., UFF, a Full Periodic-Table Force-Field for Molecular Mechanics and Molecular-Dynamics Simulations. *J. Am. Chem. Soc.* **1992,** *114* (25), 10024-10035.
113. Ioannidis, E. I.; Gani, T. Z. H.; Kulik, H. J., molSimplify: A Toolkit for Automating Discovery in Inorganic Chemistry. *J. Comput. Chem.* **2016,** *37* (22), 2106-2117.
114. O'Boyle, N. M.; Morley, C.; Hutchison, G. R., Pybel: A Python Wrapper for the OpenBabel Cheminformatics Toolkit. *Chem. Cent. J.* **2008,** *2*, 5.
115. O'Boyle, N. M.; Banck, M.; James, C. A.; Morley, C.; Vandermeersch, T.; Hutchison, G. R., Open Babel: An Open Chemical Toolbox. *J. Cheminf.* **2011,** *3*, 33.
116. Adamo, C.; Barone, V., Toward Reliable Density Functional Methods Without Adjustable Parameters: The PBE0 Model. *J. Chem. Phys.* **1999,** *110* (13), 6158-6170.

117. Weigend, F.; Ahlrichs, R., Balanced Basis Sets of Split Valence, Triple Zeta Valence and Quadruple Zeta Valence Quality for H to Rn: Design and Assessment of Accuracy. *Phys. Chem. Chem. Phys.* **2005,** *7* (18), 3297-3305.
118. Neese, F., Software update: the ORCA program system, version 4.0. *Wiley Interdiscip. Rev.: Comput. Mol. Sci.* **2018,** *8* (1), e1327.
119. Grimme, S.; Antony, J.; Ehrlich, S.; Krieg, H., A consistent and accurate ab initio parametrization of density functional dispersion correction (DFT-D) for the 94 elements H-Pu. *J. Chem. Phys.* **2010,** *132* (15), 154104.
120. Grimme, S.; Ehrlich, S.; Goerigk, L., Effect of the Damping Function in Dispersion Corrected Density Functional Theory. *J. Comput. Chem.* **2011,** *32* (7), 1456-1465.
121. Warwicker, J., pKa Predictions with a Coupled Finite Difference Poisson–Boltzmann and Debye–Hückel Method. *Proteins: Structure, Function, and Bioinformatics* **2011,** *79* (12), 3374-3380.
122. Barone, V.; Cossi, M., Quantum Calculation of Molecular Energies and Energy Gradients in Solution by a Conductor Solvent Model. *J. Phys. Chem. A* **1998,** *102* (11), 1995-2001.
123. Riplinger, C.; Neese, F., An efficient and near linear scaling pair natural orbital based local coupled cluster method. *J. Chem. Phys.* **2013,** *138* (3), 034106.
124. Riplinger, C.; Sandhoefer, B.; Hansen, A.; Neese, F., Natural triple excitations in local coupled cluster calculations with pair natural orbitals. *J. Chem. Phys.* **2013,** *139* (13), 134101.
125. Zhong, S. J.; Barnes, E. C.; Petersson, G. A., Uniformly convergent n-tuple-zeta augmented polarized (nZaP) basis sets for complete basis set extrapolations. I. Self-consistent field energies. *J. Chem. Phys.* **2008,** *129* (18), 184116.
126. Neese, F.; Valeev, E. F., Revisiting the Atomic Natural Orbital Approach for Basis Sets: Robust Systematic Basis Sets for Explicitly Correlated and Conventional Correlated ab initio Methods? *J. Chem. Theory Comput.* **2011,** *7* (1), 33-43.
127. Helgaker, T.; Klopper, W.; Koch, H.; Noga, J., Basis-set convergence of correlated calculations on water. *J. Chem. Phys.* **1997,** *106* (23), 9639-9646.
128. Lu, T.; Chen, F. W., Multiwfn: A multifunctional wavefunction analyzer. *J. Comput. Chem.* **2012,** *33* (5), 580-592.

TOC Graphic

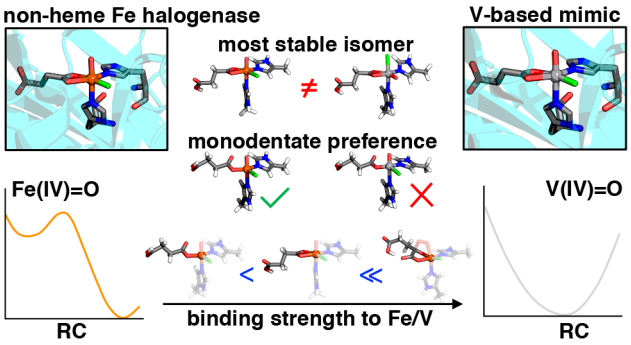
non-heme Fe halogenase
V-based mimic
most stable isomer
≠
monodentate preference
Fe(IV)=O
V(IV)=O
<
≪
binding strength to Fe/V
RC
RC